CME Interaction with Coronal Holes and their Interplanetary Consequences

N. Gopalswamy[1], P. Mäkelä[1,2], H. Xie[1,2], S. Akiyama[1,2], and S. Yashiro[1,2]
[1]NASA Goddard Space Flight Center, Greenbelt, MD, USA
[2]The Catholic University of America, Washington, DC, USA

(Accepted for Publication in JGR Space Physics, November 14, 2008)

A significant number of interplanetary (IP) shocks (~17%) during cycle 23 were not followed by drivers. The number of such "driverless" shocks steadily increased with the solar cycle with 15%, 33%, and 52% occurring in the rise, maximum, and declining phase of the solar cycle. The solar sources of 15% of the driverless shocks were very close the central meridian of the Sun (within ~15°), which is quite unexpected. More interestingly, all the driverless shocks with their solar sources near the solar disk center occurred during the declining phase of solar cycle 23. When we investigated the coronal environment of the source regions of driverless shocks, we found that in each case there was at least one coronal hole nearby suggesting that the coronal holes might have deflected the associated coronal mass ejections (CMEs) away from the Sun-Earth line. The presence of abundant low-latitude coronal holes during the declining phase further explains why CMEs originating close to the disk center mimic the limb CMEs, which normally lead to driverless shocks due to purely geometrical reasons. We also examined the solar source regions of shocks with drivers. For these, the coronal holes were located such that they either had no influence on the CME trajectories, or they deflected the CMEs towards the Sun-Earth line. We also obtained the open magnetic field distribution on the Sun by performing a potential field source surface extrapolation to the corona. It was found that the CMEs generally move away from the open magnetic field regions. The CME-coronal hole interaction must be widespread in the declining phase, and may have a significant impact on the geoeffectiveness of CMEs.

1. Introduction

It is well known that coronal mass ejections (CMEs) arriving at Earth generally originate close to the disk center (within the longitude range of ±30°) of the Sun [see, e.g., *Bravo and Blanco-Cano*, 1998; *Gopalswamy et al*., 2000a; *Cane and Richardson*, 2003]. CMEs originating at larger central meridian distances can deliver only a glancing blow to Earth, so one observes just the shock or shock with sheath at the CME flank. When viewed without the solar connection, such interplanetary (IP) shocks will appear as "driverless" shocks. Just a decade ago, the origin of such shocks was a mystery [*Schwenn*, 1996], but extensive observations of CMEs and their IP counterparts over the past decade have revealed that these shocks are also CME driven but the driver does not arrive at the observer because of the observer's location with respect to the nose of the CME [see, e.g. *Gopalswamy et al*., 2001a; *Gopalswamy*, 2006a]. Such geometrical considerations fit well with the observed variation of geoeffectiveness of halo CMEs [*Howard et al.*, 1982] with their solar source longitude: CMEs originating from close to the disk center have high rate of geoeffectiveness, while those from close to the limb have only a moderate rate. In order to explain the deviations from this pattern, *Gopalswamy et al*. [2007] mentioned propagation effects that deflect the CMEs away from the Sun-Earth line. CME deflection has been reported when CMEs collide with each other [*Gopalswamy et al*., 2001b]. CME deflections can also be caused by coronal holes (CHs), which are regions of high Alfven speed. Such deflections can move a CME closer to the Sun-Earth line [*Gopalswamy et al.*, 2005a] or away from it [*Gopalswamy et al*., 2004] depending on the relative location of the CH and the CME source with respect to the observer. These suggestions were based on case studies and detailed investigations have not been performed except for the large-scale deflection by the global solar magnetic field [*Gopalswamy et al.*, 2000b; *Filippov et al.*, 2001; *Gopalswamy et al*., 2003c; *Cremades et al.*, 2006]. In this paper, we consider the solar sources of CMEs responsible for the IP shocks of solar cycle 23 to isolate a subset of shocks that have their sources near the disk center, yet the CMEs did not arrive at 1 AU. We present detailed observational evidence which confirm that CHs are indeed responsible for the deflection of disk-center CMEs away from the Sun-Earth line. Disk-center CMEs without shock drivers at 1 AU preferentially occurred during the declining phase of the solar cycle, when low latitude CHs appear frequently. We further confirm this result by examining the coronal environments of all the shock-driving disk-center CMEs during the declining phase of solar cycle 23.

2. Shocks of Solar Cycle 23

Since CME observations are crucial to our study, we chose the first 11 years of operation of the Solar and Heliospheric Observatory (SOHO) mission (1996-2006, inclusive). SOHO has been providing information on CMEs almost continuously since its launch in 1995, except for a few-month break in 1998 (June to October). We compiled all the IP shocks detected during this period by at least one of the three spacecraft, viz., SOHO, Wind, and the Advanced Composition Explorer (ACE). Preliminary lists of shocks are available at the web sites of observing spacecraft: Wind (http://lepmfi.gsfc.nasa.gov/mfi/ip_shock.html), ACE (http://www-ssg.sr.unh.edu/mag/ace/ACElists/obs_list.html#shocks), and SOHO (http://umtof.umd.edu/pm/FIGS.HTML). After carefully eliminating shocks associated with corotating interaction regions (CIRs), we arrived at a list of 225 shocks, all of which had overlapping SOHO observations. We also determined whether the shocks are followed by IP CMEs (ICMEs) or not. When a shock is followed by an ICME, we refer to it as a "shock with driver". If there is no discernible driver, we refer to it as a "driverless shock". We would like to make it clear that a driverless shock does not mean there is no driver: the driving CME propagates at large angles to the Sun-Earth line and hence is not intercepted by the observing spacecraft. The list of shocks and the driving ICMEs, along with the associated white-light CMEs, flares and radio emission characteristics will be published elsewhere [*Gopalswamy et al*., 2008, under preparation]. Here we are concerned with the solar source locations of the associated CMEs and their coronal environment.

2.1 Identification of ICMEs

There are many signatures in the solar wind for identifying the ICME driver (see, e.g., *Neugebauer and Goldstein*, 1997). Of these, magnetic field and solar wind plasma signatures are often used. The magnetic field enhancement, smooth rotation of the field along the trajectory of the observing spacecraft, and low proton temperature (or beta) are the best signatures of magnetic clouds (MCs), which are a subset of ICMEs (Burlaga et al., 1981). Since our main concern is the existence of ICME behind the shock or not, we use a simplified scheme to determine the existence of ICMEs behind shocks. We plot the magnetic field magnitude (Bt) and its Y and Z components (By, Bz), solar wind bulk flow speed (V), proton temperature (Tp), and the alpha to proton density ratio (Nα/Np). We use ACE data in GSE coordinates. The time resolution is 4 min for the magnetic field data and 64 s for V, Tp, and Nα/Np. We also plot the expected solar wind proton temperature (Texp) from Lopez and Freeman (1986) and Neugebauer et al. (2003). From these plots, we identify the intervals of Tp depression with respect to Texp. Ejecta intervals are those with Tp/Texp <0.5 (Cane and Richardson, 2003;

Neugebauer et al., 2003; Elliott et al., 2005). We also use Nα/Np >0.08 as a secondary criterion to cross check the Tp depression. We also check if the magnetic field is enhanced with respect to the normal solar wind value. When the Tp depression is marginal (0.5 < Tp/Texp <1) in an interval but accompanied by Nα/Np >0.08 during at least part of the interval, we regard that interval to be an ejecta.

Figure 1 shows one of the shocks followed by a driver (MC in this case). The shock at 02:19 UT on 2005 May 15 can be readily recognized from the plots of solar wind and magnetic field parameters obtained by the ACE spacecraft. Immediately after the shock, the Tp is enhanced in the sheath, which is a ubiquitous signature of all the shocks irrespective of the existence of ICME signatures. The sheath lasts for ~15 h in this case. Depression of Tp below 0.5Texp marks the onset of the ICME (09:15 UT). Nα/Np was definitely enhanced with respect to the pre-shock values, but the enhancement is not above 0.08. The Tp depression ends at the end of the day. Thus the duration of the MC is ~15 h. Based on the magnetic signatures, the onset of the MC was determined to at 05:42 UT as reported in the web site of Magnetic Field Investigation [Lepping, et al., 1995] on board Wind. The onset at 09:15 UT makes the MC to be a unipolar (Bz points to the north throughout the MC interval). The cloud is also of high inclination since the smooth rotation is in the east-west direction. This example illustrates the typical sequence observed at 1 AU: the shock, the sheath interval (Tp > Texp), and ejecta (Tp <0.5Texp).

Figure 2 shows the magnetic field and solar wind properties around two shocks that are not followed by a driver. The shocks arrive at 01:47 UT on 2004 April 9 and 19:25 UT on April 10. Both the shocks have an enhanced Tp region immediately following the shock. The Tp drops to Texp after 22 h in both cases. Note that Tp does not drop below Texp. Nα/Np is also very low during the enhanced Tp. We call the interval between the shock and the time when Tp starts tracking Texp as "sheath". The sheath is normally defined as the interval between the shock and ejecta, which has a typical extent of ~13 h [e.g., *Gosling et al.*, 1987]. Thus the true sheath interval may be different because the observing spacecraft does not pass through the ejecta. Comparing Figs. 1 and 2, we see that the shock – sheath – ejecta sequence is truncated after the first two for the driverless shocks.

2.2 Identification of Solar Sources

Each IP shock is uniquely associated with a CME observed by SOHO's Large Angle and Spectrometric coronagraph [LASCO, *Brueckner et al.,* 1995]. The association is usually made by examining all CMEs that occurred over a window of 0.5 to 5 days prior to the shock arrival time at 1 AU. The solar source location of a CME is defined as the heliographic coordinates of the associated eruption: H-alpha flare location if available from the Solar Geophysical Data or the location of an associated disk activity such as EUV dimming or post eruption arcades [see *Gopalswamy et al.*, 2007 for details on CME source identification]. Since the CMEs we are concerned with are expected to drive shocks to large distances from the Sun (at least to 1 AU), we give preference to more energetic CMEs (faster and wider on the average).

Figure 3 illustrates the method of identifying the CME-IP shock pairs using the 2005 May 15 event described in Fig. 1. Recall that the MC arrived at ~ 09:15 UT on May 15 preceded by the shock at 02:19 UT. The shock and ejecta were of very high speeds (962 km/s and 875 km/s, respectively), so the CME at the Sun has to be within about two days before the shock arrival. There is a small ACE data gap near the time, so we obtained the speed from the SOHO's Mass Time of Flight Spectrometer (MTOF) data. When we examined LASCO data for 0.5 to 2 days before the shock arrival time, we found a fast (1689 km/s) halo CME starting at 17:12 UT on May 13. The CME onset time near the solar surface was estimated to be ~16:48 UT by extrapolating the height-time measurements. The actual onset time is likely to be earlier because the height time measurements made in the sky plane are subject to projection effects. In fact, *Yurchyshyn et al.* [2006] reported that the eruption began at ~16:03 UT based on H-alpha observations of the filament [see also *Liu et al.*, 2007]. The CME originated from slightly east of the central meridian, in the northeast quadrant (N12E11), as seen in the 16:32 UT EUV difference obtained by the Extreme-ultraviolet Imaging Telescope [EIT, *Delaboudinère* et al., 1995] on board SOHO. In the next image at 17:07 UT, the EUV disturbance had covered the whole solar disk, consistent with the halo CME seen by LASCO at 17:22 UT. The eruption was associated with a M8.0 flare in active region (AR) NOAA 0759. Given the high speed of the CME and its location close to the disk center, there is no ambiguity in connecting the CME at the Sun and the shock at 1 AU. A type II burst in Fig. 3, observed by the Radio and Plasma Wave Experiment [WAVES, *Bougeret et al.,* 1995] on board Wind, shows continuity between the shock near the Sun and the shock detected in situ. Type II bursts also provide evidence for the CME-driven shocks in the IP medium, before they are detected in situ. From the onset of the eruption at the Sun (~16:03 UT) to the shock arrival at 1 AU (2:19 UT on May 15), the shock

travels ~34 h. Thus the transit speed is ~1200 km/s, consistent with the initial speed of 1689 km/s and the 1-AU speed of 962 km/s. The type III burst shown in Fig. 3 also roughly marks the onset of the eruption. A similar procedure was employed to obtain the information on the source location of CMEs associated with the shocks. This is a fairly isolated event, so the identification of the solar source is rather straightforward. However, when the activity is high, there may be multiple shocks and CMEs in quick succession. In such cases, we have to carefully establish a time ordering of the shocks and CMEs. When there are two shocks and two CME candidates, the time order will be maintained if the second CME is slower than the first CME since so we do not expect the second CME to catch up with the first one. This means the shocks ahead of these CMEs will arrive in the same time sequence as their origin at the Sun. For the shocks used in this paper, the identification is not very complicated.

3. Solar Source Distributions

Table 1 summarizes the number of shocks and the shock occurrence rate (per year) for the three phases of solar cycle 23: rise (May 1996-December 1998), maximum (January 1999- May 2002), and declining (June 2002 – December 2006) phases. The division of the phases is not very rigid, especially the maximum phase. We have defined the end of the maximum phase as the time when the polarity reversal was complete at both poles [see *Gopalswamy et al.,* 2003a]. The declining phase should end in December 2007 when a definite active region of the new cycle appeared. However, the period (June 2002 to the end of 2006) we have considered should be representative of the declining phase. The number of shocks varies with the solar cycle similar to other energetic phenomena such as the large solar energetic particle events, fast-and-wide CMEs, and IP type II radio bursts [see, e.g., *Gopalswamy et al.*, 2003b; *Gopalswamy*, 2006b]. The number of shocks with drivers has a similar variation. However, the number of driverless shocks steadily increases from the rise phase to the declining phase. The driverless shocks constitute ~17% of all shocks. We have also given the number of shocks with the associated CMEs originating within a central meridian distance of ~15°. We study these disk-center shocks in this work.

3.1 Driverless Shocks from the Disk Center

Figure 4 shows the distribution of solar source locations of CMEs identified to be responsible for the shocks at 1 AU. Sources of shocks with ejecta (diamonds) and driverless shocks (circles) are distinguished in the plots. The following are evident from Figure 4: (1) the source latitudes are relatively high in the rise phase compared to the maximum and declining phases. This is simply a consequence of the locations on the Sun at which active regions emerge following the familiar butterfly diagram (the so-called active region belt). (2) The number of shocks is the largest during solar maximum and least during the rise phase. This is directly related to the increased solar activity during solar maximum as evidenced by the Sunspot number or the CME daily rate. (3) The sources of shocks with ejecta cluster around the central meridian and the number and tapers off towards the limbs. (4) Sources of CMEs associated with driverless shocks are generally close to the limb, as expected because of geometrical reasons: shocks are more extended than the driving ICMEs, so an observer along the Sun-Earth line is likely to pass through the shock flanks but not through the drivers. Such close-to-the-limb sources can be found in all the three phases. However, there are five CME sources associated with driverless shocks but located close to disk center (within the longitude range of -15° to +15°). What is remarkable is that all such disk-center eruptions resulting in driverless shocks occurred only during the declining phase (see also Table 1). In Fig.5, we have plotted just the sources of driverless shocks, distinguishing the disk-center ones by the encircled symbols. There was also a single driverless shock source (enclosed by a square) close to the disk center during the maximum phase, but well outside the 15° central meridian distance. The corresponding CME occurred on 2001 March 24 at 20:50 UT originating from AR 9390 located at N15E22 and resulted in a driverless shock on 2001 March 27 at 02:02 UT.

Geometrical considerations require that large CMEs originating from the disk center arrive at Earth with all the substructures – shock, sheath, and the driving ejecta. So, why do these five CMEs buck this trend? The clue to answer this question comes from the fact that the driverless disk-center shocks are confined to the declining phase of the solar cycle (the first one occurred on 2003 April 24 at 18:19 UT from a CME on April 21 at 13:36 UT originating from N18E02. See Table 2 for the list of all driverless shocks). During the declining phase, CHs occur quite frequently at low-latitudes. CHs are large-scale structures on the Sun with distinct physical and magnetic properties and are known to be source of high-speed solar wind. Therefore, we hypothesize that in the case of driverless shocks with disk-center CME sources, there must be intervening CHs that affect the radial propagation of CMEs such that they are deflected away from the Sun-Earth line. In the next two subsections, we examine the coronal environment of CMEs originating close to the disk center but manifest as shocks with and without drivers at 1 AU.

3.1. Source Environment of Driverless Shocks

Figure 6a illustrates the coronal environment of the 2003 November 20 CME, which resulted in a driverless shock on November 22 at 09:59 UT. The halo CME originated from AR 0501 at N01W08 and had a speed of 669 km/s measured along PA 219°. CHs are outlined using a single contour at 50% of the median intensity of the solar disk in EUV as observed by SOHO EIT in the 284 Å band. CHs are observed best in soft X-rays, but we use the SOHO EIT in the 284 Å images, which are similar to soft X-ray images because of data availability for almost all the events. One can also use the He 10830 Å images available from Kitt Peak National Observatory, but there were large data gaps during our study period. The He 10830 Å maps are also available only once a day (around 16 UT), so the time difference between the CME onset and CHs may be very large. In fact, He10830 Å maps are available only for ~one third of the events considered here. In defining the CH boundaries, we made use of the magnetograms obtained by SOHO's Michelson Doppler Imager (MDI) in eliminating areas within the CHs that had minority magnetic polarity. We also eliminated areas of nearby filaments (if any), which also appear dark in the EIT images. The largest CH in Fig. 6a located the northeast (NE) quadrant has its centroid at N16E10. The centroid is at a distance of 2.9 x 10^5 km from the eruption site (N01W08). Since the CME is expected to impact the CH boundary closest to the eruption region first, we also measured the distance D from the eruption region to the CH boundary. In Fig. 6a, we see that the CH border is much closer to the eruption region (distance D = 9° heliographic) than the centroid. Figure 6b shows that the photospheric magnetic field of this CH (from SOHO/MDI) has a negative polarity.

We calculate an "influence parameter" f for each CH, similar to the fictitious force used by *Cremades et al.* [2006], except that we include the strength of the magnetic field in the CH. We assume that f acts in the direction from the CH centroid to the eruption region and is proportional to (i) the CH area A, (ii) the average magnetic field at the photospheric level <B>, and (iii) the inverse square of the distance (r) between the CH and the eruption region. Thus, $f \sim <B>A/r^2$, which has the dimension of G. The CH area is measured from the EIT 284 Å, which is the area enclosed by the contour at 50% of the EUV intensity of the solar disk. The average magnetic field in the coronal hole is obtained from the SOHO/MDI magnetograms obtained in the synoptic mode (one magnetogram every 96 min). The EIT 284 Å contour is superposed on the magnetogram after rotating the magnetogram to the time of the EIT image. In order to improve the signal to noise ratio, we combined three consecutive magnetograms closest to the time of eruption. We assumed that the magnetic field lines in the CH are radial and accordingly corrected the field strength and coronal-hole area using the known angle of the CH centroid with respect to the line of sight. For the N16E10 CH in Fig.6a, we get a corrected area A (in 10^9 km^2) as 75 and <B> ~-8.0 G. Using r = 2.9 x 10^5 km, we get f = 7.3 and the position angle in which f is directed (fPA) is 227°. This way, we computed the influence factors of all the coronal holes and obtained their vector sum as the resultant influence factor F. For example, the smaller CH to the south (centroid at S13E23) is at a distance of 4.1 x10^5 km with A = 16 and <B> = -10.9, giving f = 1.0 and fPA = 296°. The CH to the north (centroid at N64E46) at a distance of 8.3 x10^5 km has A = 21 and <B> = -8.0 resulting in f = 0.25 and fPA = 201°. Finally the CH near the south pole (centroid at S70W25) located at a distance of ~8.0 x10^5 km has A = 21 and <B> = 8.7, so f = 0.29 in fPA = 6°. It is clear that the N16E10 CH is dominant by compared to all the other CHs. The net influence F of all the CHs is F = 7.8 pointed along the PA of 236°. The red arrow in Fig. 6a represents the direction of F, along FPA = 236°. Recall that the MPA of the CME is 219°, so the difference between FPA and MPA is only ~17°. In other words, the fastest moving segment of the CME seems to coincide with the direction in which the FPA acts.

Since coronal holes are supposed to contain open magnetic field lines, we performed potential field source surface (PFSS) extrapolation of the photospheric magnetic field using an IDL routine available in the SolarSoftWare (SSW) tree, which makes use of the synoptic magnetic charts constructed from SOHO/MDI magnetograms made available online by M. deRosa and K. Schrijver (http://www.lmsal.com/forecast/index.html). The magnetogram in Fig.6b is from the MDI synoptic magnetogram projected on a spherical surface close to the time of the CME. Open field lines starting from the photosphere are extrapolated to a heliocentric distance of 2.5 Rs into the corona. The red and blue lines indicate negative and positive polarity field lines, respectively. Note that there is an overall correspondence between the open field lines and the coronal holes, with differences originating from the different heights of measurements. The PFSS extrapolation shows that there is a "wall" of open field lines immediately to the east of the eruption region extending from the north pole to the southeast limb. The predominant motion of the CME is away from the N16E10 CH, in the southwest direction as indicated by the arrow extending from the solar disk center and marking the MPA (219°) of the CME. This observation is strongly suggestive that the open field lines in the CH are responsible for deflecting the CME away from the Sun-Earth line. Interestingly, the same region (AR 0501) produced another halo CME two days earlier (2003 November 18) when it was at S01E33, resulting in a shock with driver (a magnetic cloud) at Earth and caused the largest geomagnetic storm of cycle 23 [see *Gopalswamy et al*., 2005a]. The N16E10 CH discussed above was also present on November 18, to the east of the eruption region. The November 18 CME was also constrained to move in the SW direction, closer to the Sun-Earth line because of the CH location. The trajectories of both CMEs are affected by the same CH, but the consequences are

different because of the different locations of the CH and eruption region with respect to the disk center: the November 18 CME was deflected closer to the Sun Earth line, while the November 20 CME was deflected away from it.

Figure 6b shows another interesting fact: the N16E10 CH extends all the way to the trailing polarity patch of the eruption region. In fact, intense open field lines can be seen in the negative polarity patch of the active region. The dense field lines in the southeast limb also seem to originate from the negative polarity region of another active region. However, the coronal hole contour selected based on the criterion that it should enclose EUV intensity less than 50% of the disk intensity does not extend all the way to the negative polarity patch in AR 0501, where the open field strength may be higher. The f values computed using the EIT area, therefore, may have some uncertainty. Another point to note is that the no coronal hole was selected corresponding to the active region near the southwest limb by the criterion. The main reason again is the obscuration by foreground coronal structures. Importance of the PFSS extrapolation in providing a consistency check will be further discussed below.

In order to see if the influence of the CHs is significant in other cases, we have shown the coronal environments of the six disk-center CMEs associated with the driverless shocks in Figure 7. In the case of the solar maximum event (2001 March 24 CME), the nearest CH is to the north, so the CME is expected to be deflected closer to the Sun-Earth line. When the influence factor was computed for all the CHs, the resultant turned out to be F = 2.5 directed along FPA = 92°. The effect of the smallest CH (centroid at S62W34) is negligible (f = 0.05), while the other two CHs had f = 1.5 (S47E12) and 2.9 (N31W12). The FPA (92°) and MPA (32°) had a difference of ~ 60°. The net influence of all the CHs seems to deflect the CME to the east and north, thus preventing the ejecta from arriving at Earth. Recall that the source location (N15E22) of the solar maximum event is only marginally close to the disk center, so even a small deflection can diminish the likelihood of the ejecta arriving at Earth. In all the five declining-phase eruptions, the CHs were located close to the eruption region such that the CMEs were deflected away from the Sun-Earth line.

The PFSS extrapolation for all the six driverless shock cases is shown in Fig.8. In every case, we see that the CME trajectory is away from the region of open field lines. The MPA and FPA are closely aligned ($d\varphi \leq 37^{\circ}$), except for the 2004 April 08 CME for which $d\varphi = 71^{\circ}$ and the solar maximum event (2001 March 24 CME) with $d\varphi = 60^{\circ}$. A closer look at the PFSS extrapolation in Fig. 8 reveals that there is a narrow part of the CH extending to the east of the eruption region, which is outside the area selected in the EIT image. We suspect that this part of the CH is partly obscured by the foreground emission from the active region loops. Taking this region of open field lines into account will move the FPA closer to the MPA. Note that the previous event on 2004 April 6 is also from the same active region ($d\varphi = 37^{\circ}$) and might have been subject to similar projection effects. The PFSS map in Fig. 8 for the 2001 March 24 also shows dense open field lines extending to the north and east of the large southern coronal hole. These field lines are located in a coronal hole, which was not selected by the criterion used because of its location close to t he limb. When we take the open field lines into account we expect that the FPA and MPA would be more closely aligned.

Another interesting point to note is that all the declining-phase active regions in Fig. 8 have open filed lines in one of their polarity patches, which appear as a continuation of the open field lines in the nearby coronal holes. The PFSS plot did not show open field lines for the source active region of the 2001 March 24 CME. Although the sample is small, it is significant that 5 out of 6 source regions (or 83%) had open field lines (see Fig. 8). Solar wind from such active region open field lines has been extensively investigated (see e.g., Liewer et al., 2004).

Figure 9 shows SOHO/LASCO white light images of the CMEs corresponding to the six eruptions in Figs. 7 and 8. The measurement position angles are the marked by arrows. The source regions of the CMEs can also be seen in EUV difference images (SOHO/EIT at 195 Å) superposed on the white-light images. There was no EIT observation for the 2003 April 21 CME, so the flare location obtained from the Solar Geophysical Data is indicated by the 'x' in the figure. Although the CMEs do not appear as halos in these images, they eventually became full halos in the LASCO/C3 images, except for the 2003 April 21 CME. However, this CME is already faint, so it is difficult to say whether it is halo or not from LASCO/C3 images. The CME on 2004 December 3 is already a halo in the C2 images. The main point is that the brightest parts of the CMEs generally move away from the CHs (or regions of open field lines), consistent with the suggestion made above that the CMEs is constrained to move away from the Sun-Earth line.

Table 2 summarizes various parameters of the six eruptions and CHs described above: the date and time in yyyy/mm/dd hhmm format (column 1); the sheath interval in hours (column 2) measured from the shock time to the time when Tp starts tracking Texp; the corresponding white-light CMEs (date and time of first appearance of the CME in mm/dd hhmm

format in column 3); the heliographic coordinates of the eruption regions (column 4); the average sky-plane speed of the CMEs obtained from LASCO observations (column 5); the measurement position angle (MPA in degrees) of the CMEs (column 6); the PA (in degrees) in which the resultant influence (F) of the CHs act (FPA in column 7); the difference (dφ) between MPA and FPA in degrees (column 8); the resultant influence parameter of all the CHs present on the disk (F in column 9); the shortest distance D to the nearest CH (in heliographic degrees, column 10); and the minimum value of the Dst index within a day after the shock arrival (column 11). Two events occurred in 2003 and three in 2004, both years being in the early declining phase. The single solar-maximum event for which the solar source is not within ±15° but not too far is included in order to illustrate the generality of the phenomenon we are describing. As we demonstrated in Fig.2, none of the shocks was followed by a discernible driver. In only one case (2004 April 24 event), there was a small interval (< 2h) during which there were two little drops of Tp below 0.5 Texp (each lasting for ~30 min). It is possible that there was a small ICME material during this interval. Most of the CMEs were halos, consistent with their origin near the disk center. The sheath intervals are typically larger than the single non-halo CME on 2003 April 21 was a partial halo with a width of 163°. The sky-plane speeds ranged from 669 km/s to 1368 km/s, with an average value of 1002 km/s, very similar to the average speed of all halo CMEs of cycle 23 [*Gopalswamy et al.*, 2007]. D varied between 3° and 24° with an average value of ~12° (or 0.2 Rs). The CHs are large with their sizes in the EUV images generally exceeding the size of the active region from which the CMEs originated. The last column in Table 2 shows that none of the CMEs was geoeffective. The Dst index ranged from -5 nT to -40 nT not reaching the -50 nT to be regarded as geoeffective. The single case of -80 nT is actually the recovery phase of the super storm on 2003 November 20. Therefore, we conclude that the presence of the CH is the primary reason for the shock-drivers not intercepted by the observing spacecraft so the shocks appear driverless.

3.2. Source Environment of Shocks with Drivers

In the above subsection we showed that all the disk-center driverless shocks occurred in the declining phase because CHs are common place during this phase. However, there were also 18 other shocks in the declining phase with drivers at 1 AU and their solar sources are close to the disk center (see Table 1). Why were the corresponding CMEs not affected by the CHs? We need to examine the coronal environments of these CMEs to understand this. One would expect that either the CHs have no influence on the CME propagation, or the direction of deflection is favorable for the CMEs to propagate more along the Sun-Earth line as we noted for the 2003 November 18 CME in section 3.1. In other words, the relative location of the CH and the eruption region with respect to the Sun-Earth line is critical.

Figure 10 shows the coronal environment of one of the disk-center eruptions (2002 May 17) resulting in an IP shock (May 20 at 03:40 UT) with a driver. This event occurred at the end of the maximum phase and is used here as an example. The solar source of the CME on 2002 May 17 at 01:27 UT is a filament eruption from S20E05. The EIT 284 Å image (Fig.10a) shows CHs close to the north and south poles. The southern group has three dark patches, as outlined by the contour at 50% of the median intensity of the solar disk in EUV. The resultant influence parameter is F= 0.69 with FPA = 16°, which deviates significantly from the MPA (145°) with dφ = 129°. The PFSS extrapolation in Fig.10b shows that open field lines emanate from the positive polarity patch of the eruption region, which seems to be an extension of the open flux in the CH (centroid at S50E28) to the southeast of the eruption region. From the PFSS open field map, we see that some regions with dense open field lines are not included within the 50% intensity area selected by the criterion, e.g., an extended region of open field lines can be seen parallel to the east limb. This region was seen in the KPNO He 10830 Å image, but not the S50E28 CH. This is a limitation of the selection criterion, which introduces some uncertainty in the computation of the influence factor. When the eastern open field region rotated on to the disk, it was observed as a CH elongated in the north-south direction with A = 9.5 and <B> = 9.7 G on 2002 May 21. Assuming that A and <B> did not change significantly, we estimated the CH centroid to be at N08E67 on May 17 and the influence factor to be 1.6 along fPA = 253°. . This value is comparable to the ones from the northern and southern CHs, which cancelled each other, so the resultant influence was due only to the eastern region (F = 1.4 along FPA = 278°). The MPA of the CME, in fact, lies between the eastern open field region and the region associated with the S50E28 CH. Based on the PFSS map we see that the S50E28 CH has more open field lines to the south of the eruption region, so it has the effect of keeping the CME closer to the Sun-Earth line. The eastern open field region also must have such confining effect. This is opposite to the effect discussed in Fig. 6. In the following, we analyze the coronal environments of all the disk-center eruptions as we did for the 2002 May 17 event.

Comment [m1]: Change

Figure 11 shows the 18 disk-center eruptions with the CHs, FPAs, and CME MPAs marked. CHs were present on the disk in every case. As for the driverless shock sources, the contours outlining the CHs are at 50% of the median intensity of the solar disk in EUV, with regions of minority polarities and dark filaments adjacent to the CHs eliminated. For one

event (2005 September 13 at 20:00 UT), there were no EIT observations for several days, so we used a He 10830 Å image taken on September 12 and rotated it to the time of the eruption. CHs are seen as bright patches at this wavelength.
One of the striking differences between Figures 7 and 11 is the distribution of dφ values. From Fig. 7, we saw that the dφ values were $\leq 37^{\circ}$ (average is just 22°) except for two events probably affected by projection effects. On the other hand, only 2 events in Fig. 11 have such low dφ values (average dφ ~87°). In other words, there is very little correspondence between FPA and MPA for the eruptions that did result in ICMEs at 1 AU, whereas two thirds of eruptions that did not result in ICMEs at 1 AU had their FPA and MPA aligned. We can infer that the CHs in Fig. 11 have an influence significantly smaller than that of CHs in Fig. 7. Another major difference between Figs. 7 and 11 is the relative location among the disk center, the eruption region, and the CH. There is no case in Fig. 11 in which the CH is located between the eruption region and the disk center, so the CMEs are not deflected away from the Sun-Earth line. In Fig. 11, the locations display the following two patterns: (i) the eruption region is located between the CH and the disk center, and (ii) the disk center is located between the CH and the eruption region. For case (i), it possible to confine the CMEs close to the Sun-Earth line, provided the influence factor is large enough. For case (ii), the CH may or may not affect the CME trajectory. Seven of the 18 eruptions (or 39%) belong to case (i): 2002 November 06, 2004 January 20, 2004 December 8, 2005 January 15 and 16, 2005 July 07, and 2005 August 31. The remaining 11 events belong to case (ii). In the case of the 2005 May 26 CME, the disk center is located between the largest CH (centroid at N11W15) and the eruption region (S08E11). When we examined the PFSS maps, we found a region of open field lines extended in the north-south direction immediately to the east of the eruption region. This region should have a confining effect on the CME. In fact, one can see this region as a dark patch in the EIT 284 Å map in Fig. 11 immediately to the left of the eruption region. This region was not reported in the He 10830 Å CH map from KPNO, but was visible in the GOES soft X-ray images available on line (http://sxi.ngdc.noaa.gov/). Thus, the 2005 May 26 event belongs to case (i) if we take the open field region into account. As we noted before, the foreground emission from the neighboring active region loops must have obscured to the CH. For a complete understanding of the trajectories of the CMEs, one has to consider a combination of CH maps and the open field distribution on the Sun because part of some coronal holes may be obscured by foreground coronal loops.

When we analyzed the PFSS extrapolation maps similar to what was done in Fig. 8, we found that open field lines were present in one of the polarity patches in the eruption regions of all but six CMEs in Table 3 (exceptions are events 3, 5, 6, 7, 8, and 9). This amounts to 66.7% of CME source regions having open field lines. When we combine this with the source regions of the 5 driverless shocks, we get 17 out of 23 (or 74%) of the CME source regions had open field lines.

Table 3 lists the18 shocks from the declining phase that had drivers intercepted at Earth. The solar sources of these shocks were close to the disk center (within $\pm 15^{\circ}$ longitude). For the 2003 August 1 event at 23:03 UT, the source longitude was 16°, but we included this in Table 3 because it is only a degree away from the $\pm 15^{\circ}$ longitude limit. The flare location is not a single point, but extended as one can infer from H-alpha or soft X-ray observations, so a few degree difference in source locations is not uncommon among different observers. In the years 2003 and 2004 the number of shocks with drivers (5 in Table 3) is the same as that without drivers (see Table 2). Table 3 has the largest number of shocks (8) in the year 2005 and a single shock in 2006, but no driverless shocks from the disk center during these two years. The entries in Table 3 are similar to those in Table 2, except that we have included the start times of ICMEs and their duration in columns 4 and 5. Table 3 gives CME time, heliographic coordinates of the solar source, CME speed, MPA, FPA, dφ, F, D, and Dst. The CME speeds were in the range 360 km/s to 2861 km/s, with an average value of 1192 km/s, similar to that of the CMEs in Table 2. Most of the CMEs were halos (11 out of 18 or 61%) or partial halos (6 CMEs had width > 120°) and one CME had a width of 102°. Several important differences between the shocks with and without drivers are evident when comparing the entries in Tables 2 and 3:
1. The CH influence parameter F has an average value of 5.8 for driverless shocks, while it is only 2.5 for the shocks with drivers. Even the smallest F value in Table 2 is larger than the average F value in Table 3. This strongly suggests that the CHs were more effective for the driverless shocks.
2. The average sheath interval of the driverless shocks is 24.2 h, compared to 14.4 h for the shocks with drivers. Sheath intervals can be large when the shock is weak or when the observing spacecraft passes through the flanks of the shocks rather than through their nose. The latter seems to be the case here (see also Lepping et al., 2008). The larger sheath intervals suggest that the nose of the shocks are deflected away from the Sun-Earth line by the coronal hole deflection.
3. The nearest coronal holes are located at larger distances (D) for shock with drivers than for the driverless shocks. D ranged from 12° to 47° (average ~ 23°) for the shocks in Table 3, while it ranged from 3° to 24° (average 12°) for the shocks in Table 2).

4. All but two of the CMEs in Table 3 were geoeffective, in contrast to no geoeffective CMEs in Table 2. The Dst values for the two non-geoeffective cases (- 28 and -30 nT) in Table 3 are close to the average value (-36.5 nT) of the last column in Table 2.
In summary, we can say that although CHs are always present at the time of eruptions in the declining phase of cycle 23, there seems to be some characteristic differences in the way they influence the CME propagation. These differences basically explain why some CHs were effective in deflecting CMEs, while the others were not.

In the above analysis we considered only the two extremes: shocks with and without a driver. We do expect intermediate situations were only a small section of the ejecta is intercepted by the observing spacecraft. The small ejecta interval at the end of the sheath in the 2003 April 24 shock may be a case where a small section of the ejecta might have been intercepted by the spacecraft. Also, the ejecta can be deflected by small amounts so that they are still intercepted by the observing spacecraft. When we plotted the ejecta duration as a function of the influence parameter we found a weak tendency that larger CH influence factors are associated with smaller ejecta intervals. The correlation coefficient is not very high (-0.23) but is consistent with the conclusion that CHs influence the propagation of CMEs.

4. Discussion and Conclusions

The primary result of this study is that the trajectory of CMEs is significantly affected when the eruptions occur in close proximity to CHs. The CH acts as a magnetic wall that constrains the CME propagation. CHs are the only large-scale magnetic features (with a scale size similar to that of CMEs near the Sun) that contain different magnetic, physical and flow properties than the active-region corona where CMEs originate. The importance of the magnetic field was considered to explain the non-radial motion of prominences and CMEs during the minimum phase of the solar cycle. Using a case study [*Gopalswamy et al*., 2000b] and a statistical study [*Gopalswamy et al*., 2003c] it was shown that CMEs have an equatorward offset of position angle compared to that of the eruptive prominence source. The non-radial motion during the rise phase of the solar cycle has been attributed to the higher magnetic field strength in the solar polar regions (where CHs are present in this phase) [*Filippov et al*., 2001]. The predominance of magnetic clouds over non-cloud ICMEs during the rise phase of the solar cycle [*Riley et al*., 2006] has also been attributed to such fields because the polar CHs are closer to active regions that produce the CMEs at higher latitudes in the beginning of the solar cycle [*Gopalswamy et al.,* 2008c]. The inconsistency between the CME position angle and the source position angle from the location of the eruptive prominence reported by *Gopalswamy et al*. [2003c] was later explained in terms of a fictitious force that depends on CH area and the distance between the CH and the eruption region [*Cremades et al.*, 2006]. The present study includes the magnetic field within the CH at the photospheric level. Unlike the effect of the polar CHs and the global solar field, here we consider the effect of low-latitude CHs in the declining phase of the solar cycle.

From Table 2 and 3, we saw that the sheaths of driverless shocks are nearly 2 times thicker than those of shocks with drivers (24 h vs. 14 h). The sheath interval can be large due to two reasons. (i) The driver may be very slow and (ii) the sheath is observed near the flank, where the shock is expected to be weak. Since the CMEs have similar average speeds in both groups of shocks, we can rule out (i). In a bow shock, the sheath thickness increases as one goes from the nose to the flanks. The difference in sheath intervals between shocks with and without drivers is thus consistent with the deflection scenario: in the case of driverless shocks, the spacecraft passing through the shock flanks (because of deflection), where the sheath interval is expected to be much longer. For shocks with drivers, the spacecraft passes through the shock near the nose, encountering shorter sheath thickness. The compression in the flank sheaths is smaller than that at the nose consistent with the different geoeffectiveness for the CMEs in Table 2 and 3.

One of the important outcomes of this study is the need to consider the open field distributions on the Sun using a technique such as the PFSS extrapolation in addition to the CH images for a better understanding of the CME trajectories. We have seen that such open field regions (especially the ones closer to the active regions or at large central meridian distances) may not be fully selected by the criterion we used because of contamination by the foreground coronal emission. For example, there may be very small regions with high average field strength missed. These regions are likely to increase the f value of the associated CHs.

In this paper, we considered the influence of coronal holes on CMEs that drive shocks. A vast majority of CMEs do not drive shocks [shock-driving CMEs constitute only ~1% of all CMEs – see Gopalswamy, 2006]. Therefore, other CMEs that do not drive shocks may also be affected by CHs when they are present near the CME source region. Magnetic clouds and non-cloud ICMEs that do not drive shocks are not uncommon in the solar wind [see, e.g., *Gopalswamy et al.*, 2000a for a list].

This paper is concerned with coronal hole deflection close to the Sun (within the first few solar radii, Rs), quite different from other coronal-hole effects such as high-speed streams causing corotating interaction regions (CIRs) [*Sheeley et al*., 1976; *Burlaga et al*., 2003]. Near the Sun, the solar wind in the CHs may not have reached its full speed. Moreover, the flow speed may be much smaller than the CME speeds at least for the events we have considered [halo CMEs are inherently energetic, see *Gopalswamy*, 2004]. CMEs are also known to expand rapidly early on with the radial speeds comparable to the expansion speeds. Most of these CMEs have coronal or IP type II bursts, so they must be driving shocks close to the Sun. We expect that the side of the CMEs approaching the CH must interact with the vertical field lines of the CHs. The CME-driven shock at the sides is expected to be quasi perpendicular and suddenly faces the CH boundary where the Alfven speed jumps to >2000 km/s [see e.g. *Esser et al*., 1999]. Outside the CH, the Alfven speed can vary anywhere from a few hundred km/s to >1500 km/s in the active region corona [*Gopalswamy et al*., 2008a,b]. The shock ahead of the CMEs weaken as they propagate into the CH because of the higher Alfven speed and get refracted to regions of lower Alfven speed regions. Refraction of coronal shocks into low Alfven speed regions has been discussed before [*Uchida*, 1968]. The shock may also become a slow shock inside the CH if it can penetrate [see e.g., *Grib et al*., 1999].

As for the CME, it is a magnetized plasma trying to penetrate the "magnetic wall" of the CH. Two possibilities can be considered, depending on the relative direction of the magnetic fields in the CME and in the coronal hole. When the magnetic fields are parallel, the CME will be deflected because the horizontal component of the CME speed (the expansion speed) is expected to be smaller than the Alfven speed in the coronal hole. On the other hand, when the CME field lines are anti-parallel to the coronal-hole field lines, magnetic reconnection is possible and some of the magnetic flux of the CME may be eroded. Indirect evidence for such a reconnection is the brightening of the coronal-hole boundary closer to the eruption. Such a process known as the interchange reconnection [*Crooker et al*. 2002] thought cause the erosion of flux ropes in the interplanetary medium [*Reinard and Fisk*, 2004].

The main findings of this investigation may be summarized as follows:
1) A significant number of IP shocks (~17%) are not followed by the driving ICMEs at the observing spacecraft. The occurrence rate of such driverless shocks did not follow the usual solar activity cycle with 15%, 33%, and 52% occurring in the rise, maximum, and declining phase of the solar cycle, respectively.
2) The solar sources of 15% of the driverless shocks were very close to the central meridian of the Sun (within ~15° in longitude), all of which occurred during the declining phase of the solar cycle. No driverless shock was found at a longitudinal distance < 22° during the rise and maximum phases.
3) The low-latitude CHs or the low-latitude extensions of polar CHs seem to deflect the CMEs away from the Sun-Earth line in such a way that only the shock arrives at Earth while the driving ICME is missed by the observing spacecraft. The predominance of driverless shocks in the declining phase is consistent with the occurrence of low-latitude CHs during this phase.
4) For shocks with drivers, the eruption regions are generally located between the disk center and the CHs. It appears that in these cases, the CMEs are either confined close to the Sun-Earth line or not significantly affected by the CHs. Unfavorable location, size, and proximity of the CHs are the reasons for CHs not affecting the CME trajectory.
5) The influence parameter computed from the CH area, the average photospheric magnetic field within the CH, and the distance between the eruption region and CH centroids over two times larger for the driverless shocks compared to the ones with drivers.
6) The direction in which the CH influence acts on the CME and the CME position angle were close to each other (within ~37°) for the CMEs associated with driverless shocks. No such relationship was found for the CMEs associated with shocks followed by drivers at 1 AU.
7) The ICME interval was found to be weakly dependent on the influence parameter with a correlation coefficient of ~ -0.23, suggesting that ICMEs must have undergone deflections to varying degrees but not completely away from the spacecraft path.
8) The majority of eruption regions (~74%) contained open field lines. Such open field regions merged into nearby CHs. In some cases, the open field regions were not selected by the criterion employed to identify CHs. A combination of CH images and the open field distribution using PFSS extrapolation might provide a better description of the source environment of CMEs.
9) None of the CMEs associated with the driverless shocks were geoeffective, suggesting that CHs play an important role in affecting the geoeffectiveness of CMEs.

Acknowledgments: We thank the SOHO, Wind and ACE science teams for making the shock data available on line. This research was supported by NASA LWS and SR&T programs. SOHO is a project of international cooperation between ESA and NASA. The authors thank the anonymous referees for critical comments, which helped improve the presentation of the paper.

References

Bougeret, J.-L., et al. (1995), Waves: The Radio and Plasma Wave Investigation on the Wind spacecraft, Space Sci. Rev., 71, 231.

Bravo, S. and X. Blanco-Cano (1998), Signatures of interplanetary transients behind shocks and their associated near-surface solar activity, Annales Geophysicae, 16, 359-369, 1998.

Brueckner, G.E., et al. (1995), The large angle spectroscopic coronagraph (LASCO), Solar Phys., 162, 357.

Burlaga, L. F., E. Sittler, F. Mariani, and R. Schwenn (1981), Magnetic loop behind an interplanetary shock: Voyager, Helios, and IMP-8 observations, J. Geophys. Res., 86, 6673.

Burlaga, L., D. Berdichevsky, N. Gopalswamy, R. P. Lepping, and T. Zurbuchen (2003), Merged interaction regions at 1 AU, J. Geophys. Res., 108, 1425

Cane, H. V. and I. Richardson (2003), Interplanetary coronal mass ejections in the near-Earth solar wind during 1996-2002, J. Geophys. Res., 108, SSH 6-1, DOI 10.1029/2002JA009817

Cremades, H., V. Bothmer, and D. Tripathi (2006), Properties of structured coronal mass ejections in solar cycle 23, Advances in Space Research 38, 461–465

Crooker, N. U., J. T. Gosling, and S. W. Kahler, (2002), J. Geophys. Res., 107, SSH 3-1, DOI: 10.1029/2001JA000236

Delaboudinière, J.-P., et al. (1995), EIT: The extreme-ultraviolet imaging telescope for the SOHO mission, Solar Phys., 162, 291.

Elliott, H. A., D. J. McComas, N. A. Schwadron, J. T. Gosling, R. M. Skoug, G. Gloeckler, and T. H. Zurbuchen (2005), An improved expected temperature formula for identifying interplanetary coronal mass ejections, J. Geophys. Res., 110, A04103, doi:10.1029/2004JA010794.

Esser, R. et al. (1999), Plasma Properties in Coronal Holes Derived from Measurements of Minor Ion Spectral Lines and Polarized White Light Intensity, Astrophys. J., 510, L63

Filippov, B. P., N. Gopalswamy, and A. V. Lozhechkin (2001), Non-radial motion of eruptive filaments, Solar Phys., 119-130.

Gopalswamy, N., (2004) A Global Picture of CMEs in the Inner Heliosphere, in The Sun and the Heliosphere as an Integrated System, edited by G. Poletto and S. T. Suess, Kluwer, Boston, Chapter 8, p. 201

Gopalswamy, N. (2006a) Properties of interplanetary coronal mass ejections, Space Science Reviews, doi: 10.1007/s11214-006-9102-1

Gopalswamy, N. (2006b) Coronal Mass Ejections and Type II Radio Bursts, N. Gopalswamy in Solar Eruptions and Energetic Particles, Geophysics monograph 165, ed. N. Gopalswamy, R. Mewaldt, and J. Torsti, American Geophysical Union, Washington DC, p.207

Gopalswamy, N. ., A. Lara, R. P. Lepping, M. L. Kaiser, D. Berdichevsky, and O. C. St. Cyr (2000a), Interplanetary acceleration of coronal mass ejections, Geophys. Res. Lett. 27, 145.

Gopalswamy, N., Y. Hanaoka, and H. S. Hudson (2000b), Structure and Dynamics of the Corona surrounding Eruptive Prominences, Adv. Space Res, 25 (9), 1851

Gopalswamy, A. Lara, M. L. Kaiser and J.-L. Bougeret (2001a), Near-Sun and Near-Earth Manifestations of Solar Eruptive Events, J. Geophys. Res., 106, 25,261

Gopalswamy, N., S. Yashiro, M. L. Kaiser, R. A. Howard and J.-L. Bougeret (2001b), Radio signatures of CME interaction: CME Cannibalism? Astrophys. J., 548, L91

Gopalswamy, N., A. Lara, S. Yashiro, and R. A. Howard, (2003a), Coronal Mass Ejections and Solar Polarity Reversal, Astrophys. J., 598, L63

Gopalswamy, N., S. Yashiro, A. Lara, M. L. Kaiser, B. J. Thompson, P. T. Gallagher, and R. A. Howard (2003b), Large solar energetic particle events of cycle 23: A global view, Geophys. Res. Lett., 30, SEP 3-1, doi: 10.1029/2002GL016435

Gopalswamy, N., M. Shimojo, W. Lu, S. Yashiro, K. Shibasaki, and R. A. Howard (2003c), Prominence eruptions and coronal mass ejections: A statistical study using microwave observations, Astrophys. J., 586, 562.

Gopalswamy, N., S. Yashiro, S. Krucker, G. Stenborg, and R. A. Howard (2004), Intensity variation of large solar energetic particle events associated with coronal mass ejections, J. Geophys. Res., 109, A12105, doi: 10.1029/2004JA010602

Gopalswamy, N., S. Yashiro, G. Michalek, H. Xie, R. P. Lepping, and R. A. Howard (2005a), Solar source of the largest geomagnetic storm of cycle 23, Geophys. Res. Lett., 32, L12S09, doi:10.1029/2004GL021639.
Gopalswamy, N., S. Yashiro, Y. Liu, G. Michalek, A. Vourlidas, M. L. Kaiser, and R. A. Howard (2005b), Coronal mass ejections and other extreme characteristics of the 2003 October-November solar eruptions, J. Geophys. Res., 110, A09S15, doi: 10.1029/2004JA010958.
Gopalswamy, N.; Yashiro, S.; Akiyama, S. (2006), Coronal mass ejections and space weather due to extreme events, Proceedings of the ILWS Workshop. Goa, India. February 19-24, 2006. Editors: N. Gopalswamy and A. Bhattacharyya, Quest Publications, Mumbai, p.79.
Gopalswamy, N., S. Yashiro, S. Akiyama (2007), Geoeffectiveness of Halo Coronal Mass Ejections, J. Geophys. Res., 112, A06112
Gopalswamy, N., S. Yashiro, H. Xie, S. Akiyama, E. Aguilar-Rodriguez, M. L. Kaiser, R. A. Howard, and J.-L. Bougeret (2008a), Radio-Quiet Fast and Wide Coronal Mass Ejections, Astrophys. J., 674, 560
Gopalswamy, N., S. Yashiro, S. Akiyama, P. Mäkelä, H. Xie, M. L. Kaiser, R. A. Howard and J. L. Bougeret (2008b), Coronal Mass Ejections, Type II Radio Bursts, and Solar Energetic Particle Events in the SOHO Era, Annales Geophysicae, in press.
Gopalswamy, N., S. Akiyama, S. Yashiro, G. Michalek, and R. P. Lepping (2008c), Solar sources and geospace consequences of interplanetary magnetic clouds observed during solar cycle 23, J. Atmospheric and Solar-Terrestrial Physics, 70, 245
Gosling, J.T., Baker, D.N., Bame, S.J., Feldman, W.C., Zwickl, R.D., Smith, E.J., 1987. Bidirectional solar wind electron heat flux events. Journal of Geophysical Research 92, 8519–8535.
Grib, S. A., S. Koutchmy, and V. N. Sazonova (1999), MHD Shock Interactions in Coronal Structures, Solar Phys., 169, 151
Howard, R. A., D. J. Michels, N. R. Sheeley Jr., and M. J. Koomen (1982), The observation of a coronal transient directed at earth, Astrophys. J., 263, L101.
Lepping, R. P., et al., (1995), The Wind Magnetic Field Investigation, Space Sci. Rev., 71, 207-229.
Lepping, R. P., C.-C. Wu, N. Gopalswamy, and D. B. Berdichevsky (2008), Average Thickness of Magnetosheath Upstream of Magnetic Clouds at 1 AU versus Solar Longitude of Source, Solar phys., 248, 125-139.
Liewer, P. C., M. Neugebauer, and T. Zurbuchen (2004), Characteristics of active-region sources of solar wind near solar maximum, Solar Phys., 223, 209-239.
Liu, C. et al. (2007), The Eruption from a Sigmoidal Solar Active Region on 2005 May 13, Astrophys. J., 669, 1372-1381.
Lopez, R. E., and J. W. Freeman (1986), The solar wind proton temperature velocity relationship, J. Geophys. Res., 91, 1701-1705.
Malandraki, O.E., D. Lario, L. J. Lanzerotti, E. T. Sarris, A. Gerranios, G., Tsiropoula, G., (2005), October/November 2003 interplanetary coronal mass ejections: ACE/EPAM solar energetic particle observations. Journal of Geophysical Research 110, A09S06.
Neugebauer, M. and R. Goldstein (1997), Particle and field signatures of coronal mass ejections in the solar wind, in: Coronal Mass Ejection, (Ed) Crooker et al., vol. 99 of Geophysical Monograph, AGU, Washington D. C., pp. 245–251.
Neugebauer, M., J. T. Steinberg, R. L. Tokar, B. L. Barraclough, E. E. Dors, R. C. Wiens, D. E. Gingerich, D. Luckey, and D. B. Whiteaker (2003), Genesis on-board determination of the solar wind flow regime, Space Sci. Rev., 105, 661.
Reinard, A. . and L. A. Fisk, (2004), Reconnection of Magnetic Field Lines near the Solar Surface during Coronal Mass Ejection Propagation, Astrophys. J., 608, 539
Riley, P., C. Schatzman, H. V. Cane, I. G. Richardson, N. Gopalswamy (2006), On the Rates of Coronal Mass Ejections: Remote Solar and In Situ Observations, Astrophys. J., 647, 648.
Schwenn, R. (1996), An Essay on Terminology, Myths and Known Facts: Solar Transient - Flare - CME - Driver Gas - Piston - BDE - Magnetic Cloud - Shock Wave - Geomagnetic Storm, Astrophys. Space Sci., 246, 187
Sheeley, N. R. Jr., J. W. Harvey, and W. C. Feldman (1976), Coronal holes, solar wind streams, and recurrent geomagnetic disturbances, 1973-1976, Sol. Phys., 49, 271.
Skoug, R. M., J. T. Gosling, J. T. Steinberg, D. J. McComas, C. W. Smith, N. F. Ness, Q. Hu, and L. F. Burlaga (2004), Extremely high speed solar wind: 29– 30 October 2003, J. Geophys. Res., 109, A09102, doi:10.1029/2004JA010494.
Uchida, Y. (1968), Propagation of hydromagnetic disturbances in the solar corona and Moreton's wave phenomenon, Solar Phys., 4, 30.

Wang, Y.-M. et al. (2006), Impact of Major Coronal Mass Ejections on Geospace during 2005 September 7-13, Astrophys. J. 646, 625–633.
Yurchyshyn, V., C. Liu, V. Abramenko, J. Krall (2006), The May 13, 2005 Eruption: Observations, Data Analysis and Interpretation, Solar phys., 239, 317-335.

Table 1. Shocks with and without drivers at 1 AU during the three phases of solar cycle

	Rise	Maximum	Declining	Total
All Shocks	36	114	75	225
Annual Rate (shocks/yr)	12.0	33.3	16.3	20.4[b]
Shocks with Drivers	30	102	55	187
Shocks with Drivers (DC[a])	14	39	18	71
Driverless shocks	6	12	20	38
Driverless shocks (DC[a])	0	0	5	5

[a]DC denotes shocks whose CMEs originated within a central meridian distance of 15°

[b]The average rate over the whole period (225 shocks in 11 years).

Table 2. List of disk-center eruptions (source longitude within ±15°) that resulted in shocks not followed by drivers (driverless shocks).

Shock (UT)	Ts (h)	CME (UT)	Source Location	Speed[a] (km/s)	MPA[b] (deg)	FPA[c]	dφ[d]	F[e]	D[f]	Dst (nT)
2001/03/27 0202	15[g]	03/24 2050	N15E22	906	H32°	92	60	2.5	13°	-5
2003/04/24 1819	27	04/21 1336	N18E02	784	305°	317	12	5.1	18°	-40
2003/11/22 0959	29	11/20 0806	N01W08	669	H219°	236	17	7.8	9°	-80
2004/04/09 0147	22	04/06 1331	S18E15	1368	H167°	130	37	4.4	5°	-35
2004/04/10 1925	22	04/08 1030	S15W11	1068	H197°	126	71	12	3°	-29
2004/12/05 0704	30	12/03 0026	N08W02	1216	H333°	355	22	3.0	24°	-30

[a]CME speed in the sky plane from straight-line fit to the height-time measurements.
[b]Measurement position angle (MPA) at which height-time data are obtained. At this angle the CME moves the fastest. All position angles are measured (in degrees) counter clockwise from solar north. The central PA (CPA) and MPA are roughly the same for non-halo CMEs. For halo CMEs (denoted by the prefix H), the CPA is not defined.
[c]The position angle at which the resultant coronal hole influence (F) is directed.
[d]The difference between MPA and FPA
[e]Magnitude of the resultant influence of all the coronal holes present on the disk
[f]Shortest angular distance (D, in heliographic degrees) from the eruption center to the nearest coronal hole.
[g]Measured until the arrival of the next event.

Table 3: List of IP shocks with drivers (ICMEs) at 1 AU, whose solar sources were within ±15° longitude. All the shocks are from the declining phase of cycle 23.

No.	Shock (Date UT)	Sh (h)	ICME (start)	Dur (h)	CME (Date UT)	Source Loc.	V km/s	MPA (deg)	FPA (deg)	dφ (deg)	F (G)	D (deg)	Dst (nT)
1	2002/07/17 1550	34	19/0130	3.75	07/15 2130	N19W01	1300	45°	355	50	4.4	20°	-28
2[a]	2002/08/01 0510	10	01/1500	7.25	07/29 1207	S10W10	562	301°	203	98	4.4	22°	-50
3[a]	2002/08/01 2305	7	02/0615	14	07/29 2330	N12W16	360	354°	223	131	5.2	24°	-100
4	2002/11/09 1820	4	09/2230	11.5	11/06 0606	S13E13	485	162°	191	29	1.4	24°	-30
5	2003/10/29 0600	2	29/0800	20	10/28 1130	S20E02	2459	H15°	174	159	1.6	34°	-383
6	2003/10/30 1620	10	31/0200	11	10/29 2054	S19W09	2029	H190°	251	61	4.8	15°	-401
7	2004/01/22 0110	7	22/0800	31	01/20 0006	S16W05	965	H224°	56	168	2.4	22°	-149
8[b]	2004/11/07 1759	5	07/2230	18.25	11/06 0206	N09E05	1111	21°	94	73	2.5	19°	-373
9	2004/12/11 1303	24	12/1330	16.5	12/08 2026	N08W03	611	H310°	233	77	1.2	24°	-61
10	2005/01/16 1100	3	16/1415	16.25	01/15 0630	N16E04	2049	H359°	113	114	0.55	15°	-70
11	2005/01/17 0715	8	17/1500	12	01/15 2306	N15W05	2861	H323°	178	145	1.8	14°	-121
12	2005/02/17 2159	17	18/1500	17.25	02/13 1106	S11E09	584	129°	218	89	5.8	12°	-90
13	2005/05/15 0219	7	15/0915	14.75	05/13 1712	N12E11	1689	H2°	42	40	0.74	23°	-263
14	2005/05/29 0915	16	30/0115	6	05/26 2126	S08E11	420	61°	114	53	1.8	18°	-136
15	2005/07/10 0256	8	10/1100	19	07/07 1706	N09E03	683	H39°	154	115	1.7	24°	-94
16	2005/09/02 1332	18	02/2045	7.25	08/31 1130	N13W13	825	H287°	191	96	3.4	17°	-76
17	2005/09/15 0825	26	16/1030	8.25	09/13 2000	S09E10	1866	H149°	100	49	1.3	47°	-86
18	2006/08/19 1039	27	20/1400	25.5	08/16 1630	S14W13	888	H161°	175	14	0.88	40°	-60

[a]These two shocks are listed in *Cane and Richardson* [2003]. However, they associate the first CME (2002 July 29 at 12:07 UT) with the second shock and they do not list any CME for the first shock.

[b]The CME probably merged with another CME (speed = 888 km/s) at 01:32 from the same source region [*Gopalswamy et al.*, 2006].

Comments:

#1 Front boundary clear in Tp, end not clear. Tp depressed to 0.8 Texp until 08:00 UT on July 19. Nα/Np has large data gaps.
#2 Boundaries clear in Tp. Tp peak and fluctuations 02/1600-1800. Nα/Np above 0.08 for a longer period.
#3 Front boundary clear in Tp, end not clear due to fluctuations (may be until August 2, 18:00 UT. Nα/Np is mainly below 0.08.
#4 Not a clear event. No Tp signature. Two peaks in Nα/Np above 0.08, but mostly above 0.06 in the stated interval. There is enhanced magnetic field and not so smooth rotation in the east-west direction.
#5 ACE data gap. However, this is a published MC event. The stated boundaries are from magnetic signatures. Boundaries differ in published works [*Skoug et al*., 2004; *Malandraki et al*., 2005].
#6 ACE data gap. However, this is a published MC. Nα/Np above 0.08. The stated boundaries are from magnetic signatures. Boundaries differ in published works [*Skoug et al.*, 2004; *Malandraki et al.,* 2005]. More details on ## 5 and 6 can be found in *Gopalswamy et al*. [2005b].
#7 Several short duration Tp peaks within the ejecta interval. Nα/Np mostly enhanced within the stated interval, but only two peaks in Nα/Np above 0.08.
#8 Clear front boundary, end is not clear. Listed end boundary is from MC list [*Gopalswamy et al*., 2008c]. Tp depressed for a longer period until 09:30 UT on November 09. Nα/Np above 0.08 throughout the stated interval.
#9 Intermittent Tp depressions: During 18 – 24 UT on December 12, there are fluctuations showing Tp/Texp > 0.5, but <1. Nα/Np peaks earlier.
#10 Short data gap at the front boundary, otherwise clear Tp signature. Short-duration Tp fluctuations. Nα/Np above 0.08.
#11 DATA GAP (ACE). OMNI data shows Tp depression below Texp. No Nα/Np data.
#12 Clear Tp signature. Na/Np mostly above 0.08.
#13 Clear Tp signature. Nα/Np below 0.08. MC event described in Fig. 2.
#14 Clear Tp signature, but two broad peaks with Tp > 0.5Texp. The duration given corresponds to the period before the first broad peak. Nα/Np is mostly above 0.08, and stays above 0.08 a bit longer.
#15 Relatively clear Tp signature. Nα/Np peak in the middle, otherwise below 0.08.
#16 Tp depression decreases at the end (1 - 4 UT on September 3). Nα/Np below 0.08.
#17 Not a clear event. Tp/Texp is ~ 0.5 between 10:30 and 18:45 UT on September 16, but definitely below 1. Additional Tp depression below Texp until 12 UT on September 17. *Wang et al*. [2006] consider the shorter interval on Sep 15 (16-18 UT) as ICME interval, which seems in the middle of the sheath. No Nα/Np signature, but Bt and By seems smooth during the ICME interval.
#18 Tp > 0.5 Texp within a well defined Tp < 0.5 Texp interval. Nα/Np below 0.08.

Figure Captions

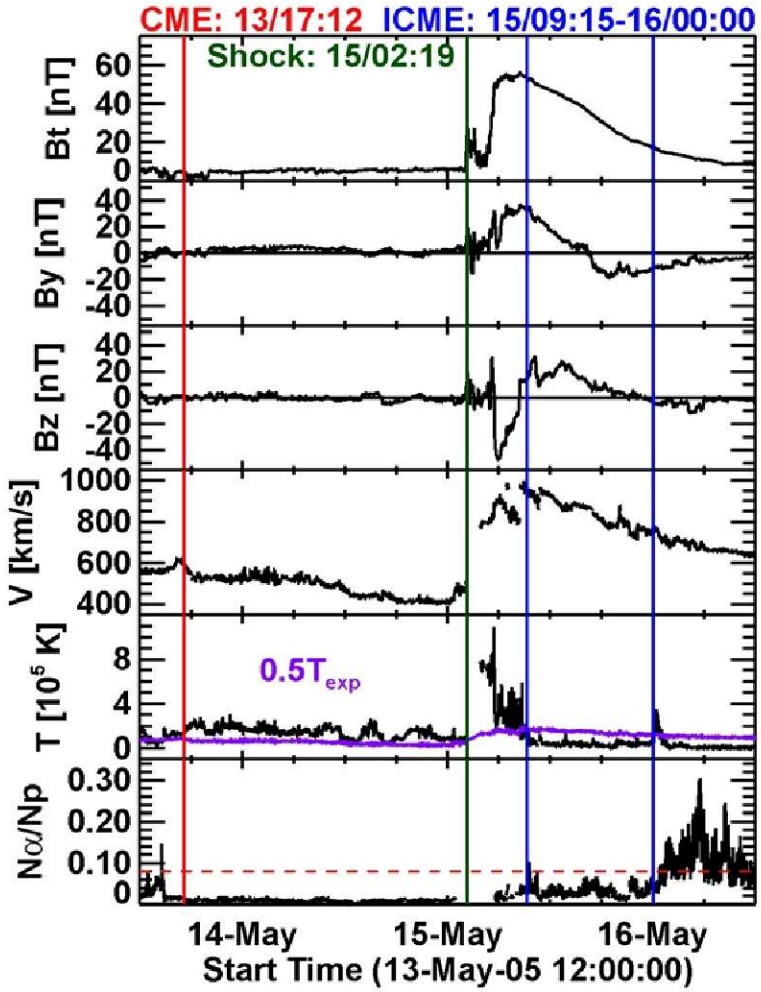

Figure 1. Magnetic and plasma parameters in the solar wind showing the interplanetary shock on 2005 May 15 at 02:19 UT: The magnitude of the magnetic field (Bt), the Y- and Z-components of the magnetic field (By, Bz), the solar wind speed (V), proton temperature (T), and the alpha-to-proton ratio (Nα/Np). The time of first appearance of the CME, the shock, and the ejecta interval (MC in this case) are marked by vertical lines. In the proton temperature plot, we have overlaid the 0.5Texp curve based on Lopez and Freeman (1986). In the Nα/Np plot, a horizontal dotted line at Nα/Np = 0.08 is included. Note that T << 0.5Texp during the marked MC interval. After a brief interval (2-3 h) enhancement, T again falls below 0.5 Texp. It is not clear if the later temperature depression is related to the MC or if it s a separate event (there is also enhanced Nα/Np during the second T depression).

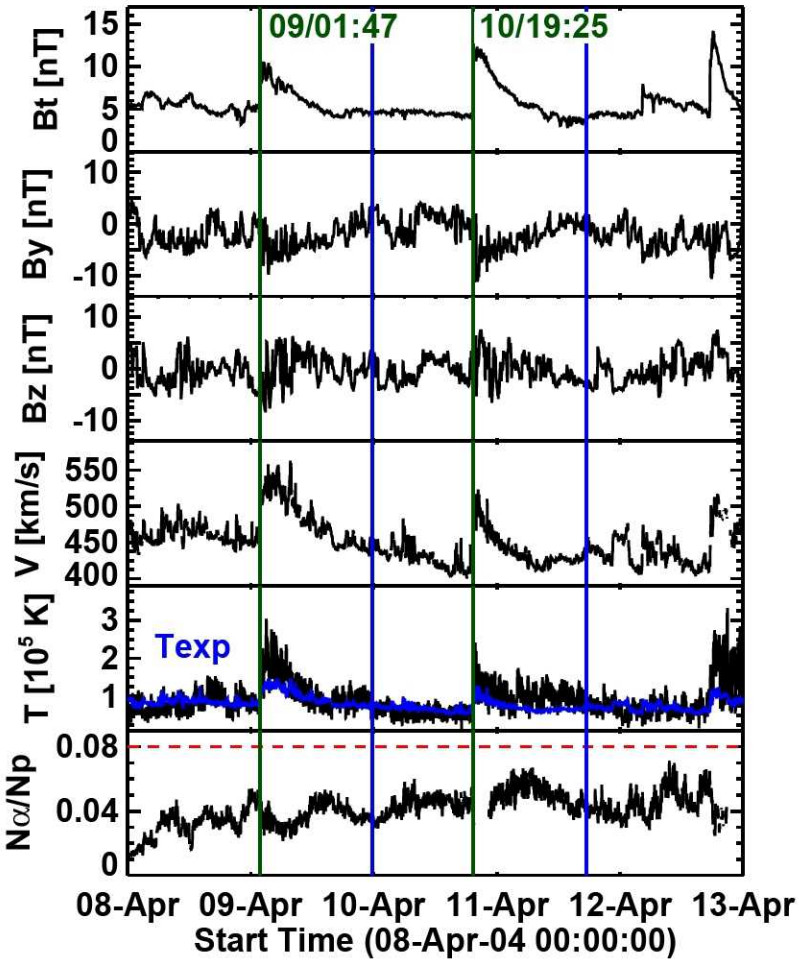

Figure 2. Magnetic and plasma parameters in the solar wind similar to those in Fig. 1, except for the interval around two driverless shocks on 2004 April 9 and 10. The shock times and the end of the sheath intervals are marked by vertical lines. The sheaths following the two shocks were of the same extent (~22 h). The sheath is defined as the interval from the shock to the time when the proton temperature decreases to the value of Texp.

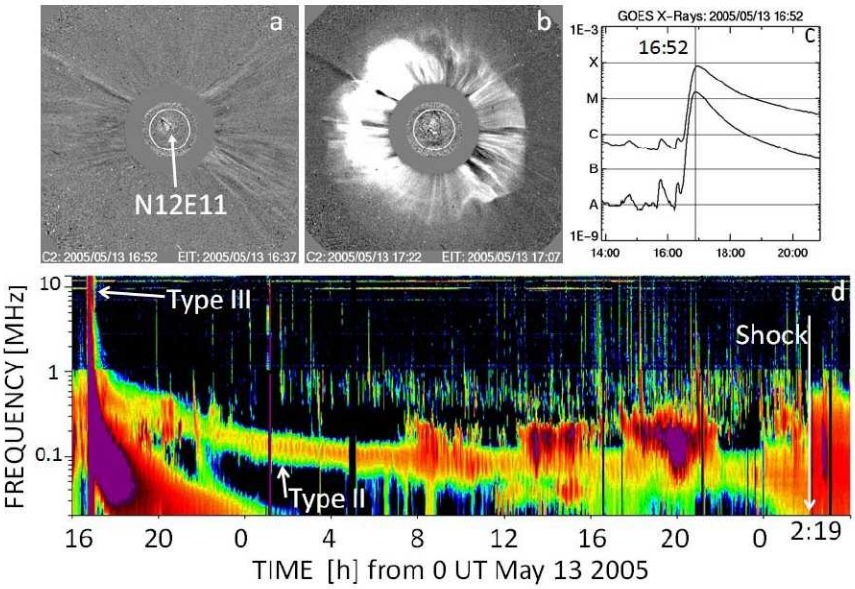

Figure 3. The SOHO/LASCO difference images at 16:52 UT (a) and 17:22 UT (b) with superposed EIT difference images at 16:37 UT and 17:07 UT, respectively showing the sudden onset of the 2005 May 13 CME. The CME was associated with an M-class flare (c) as revealed by the GOES soft X-ray data (the CME time is indicated by the vertical line on the GOES plot). The eruption was marked by a type III radio burst in the Wind/WAVES dynamic spectrum. The type II radio burst is indicative of a shock near the Sun. The radio dynamic spectrum also shows the arrival of the shock at 1 AU. The superposed SOHO/EIT image in (a) shows the solar source of the eruption.

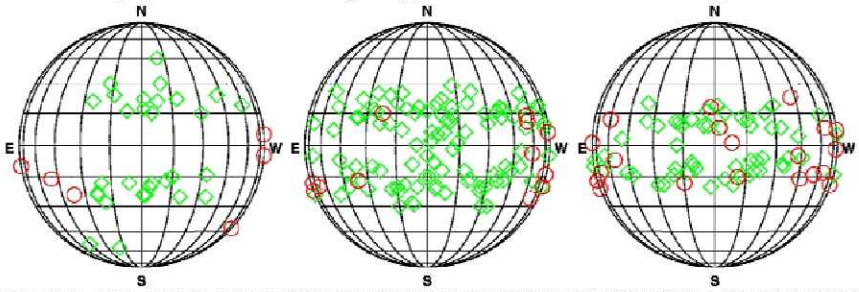

Figure 4. Locations of eruptions resulting in interplanetary shocks detected at 1 AU by spacecraft at Sun-Earth L1 Lagrange point, plotted separately for the rise (left), maximum (middle), and declining (right) phases of cycle 23. Diamonds and circles respectively denote shocks with and without drivers. Note that the "driverless" shocks generally have their solar sources near the limb during the rise and maximum phases, while they also occur near the disk center during the declining phase.

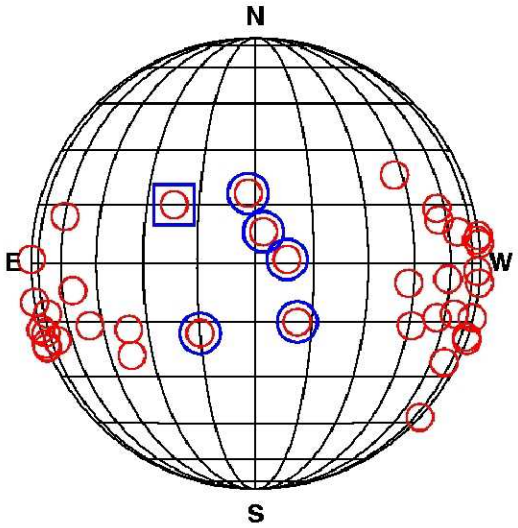

Figure 5. Solar source locations of driverless shocks from cycle 23. Sources close to the disk center (within ±15° longitude) are shown circled and are from the declining phase. The source inside the square is the single case during the maximum phase, which occurred closer to the disk center (at 22° East longitude). Note that sources of driverless shocks fall into two groups: the disk center sources and limb sources.

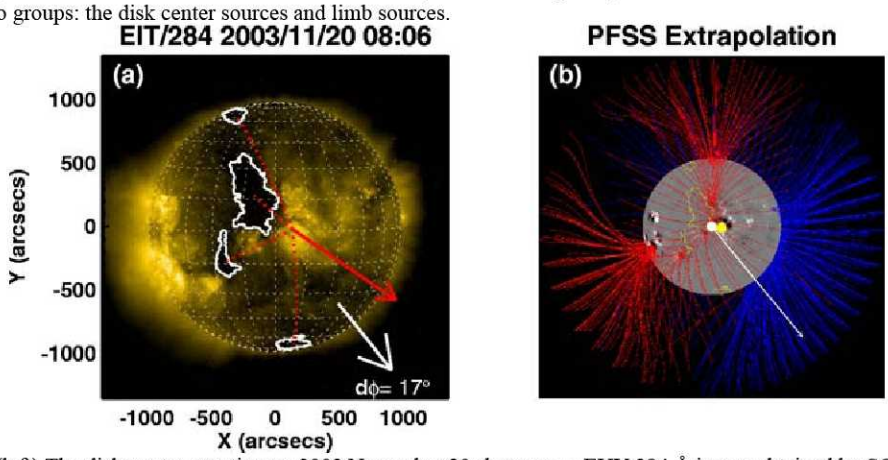

Figure 6. (left) The disk-center eruption on 2003 November 20 shown on a EUV 284 Å image obtained by SOHO/EIT. The eruption resulted in a driverless IP shock at 1 AU on November 22 at 09:59 UT. The heliographic grids are drawn with a grid spacing of 15°. The white arrow marks the position angle (PA) along which the CME height-time history was measured (i.e., MPA). The coronal holes are outlined by a single contour at the 50% level of the median EUV intensity of the solar disk, where the magnetic field is predominantly unipolar. The red dotted lines connect the eruption region to the centroids of the coronal holes. The red arrow starts from the eruption region and points in the direction of the resultant influence (F) of the four coronal holes seen on the disk. The position angle in which F points is referred to as the influence position angle (FPA). The difference (dφ) between FPA and MPA is noted on the figure (17°). (right) Potential field source surface (PFSS) extrapolation of the photospheric field to the corona up to a heliocentric distance of 2.5 Rs. Red and blue lines denote field lines pointing towards and away from the Sun, respectively. Only open field lines are shown. The photospheric field shown is made from MDI synoptic maps updated every six hours. The white arrow is along the MPA of the CME. The yellow dot marks the eruption location.

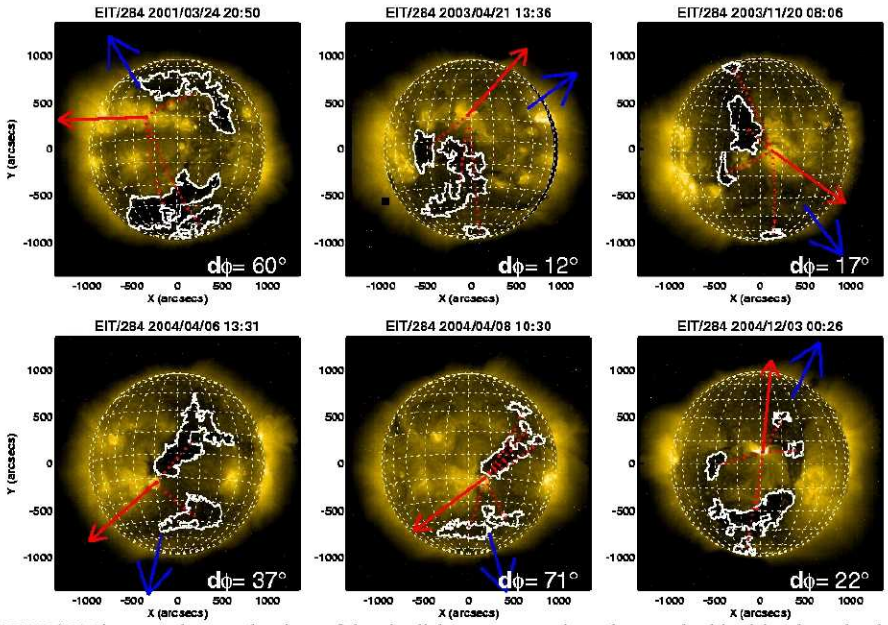

Figure 7. SOHO/EIT images close to the time of the six disk-center eruptions that resulted in driverless shocks at 1 AU. Coronal holes on the disk are outlined with a contour at 50% of the median intensity of the solar disk in the EIT image (excluding the emission above the limb). The blue arrow indicates the measurement position angle (MPA) at which the CME appeared to move the fastest and the height-time measurements were made. The red arrows denote the direction in which the resultant influence (F) of the coronal holes points (i.e., FPA). The difference (dφ) between FPA and MPA is noted on each panel. Note that the coronal holes generally intervene between the Sun-Earth line and the site of eruption.

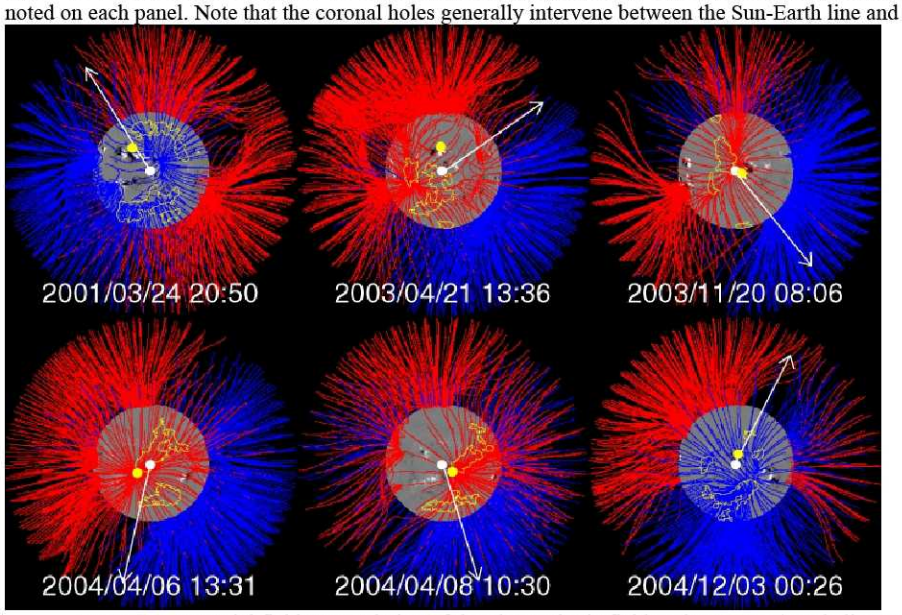

Figure 8. Potential field extrapolation of the photospheric field to the corona (to a heliocentric distance of 2.5 Rs) for the six eruptions shown in Fig. 7. Only open field lines are shown. Red and blue lines denote field lines pointing towards and away from the Sun, respectively. The white arrows denote the MPA. The white arrow

indicates the measurement position angle of the. The yello dot indicates the location of eruption. Note that open filed lines are present in all the eruption regions except for the one on 2001March 24. Also note that there are some open field lines not selected by the criterion used in defining coronal holes.

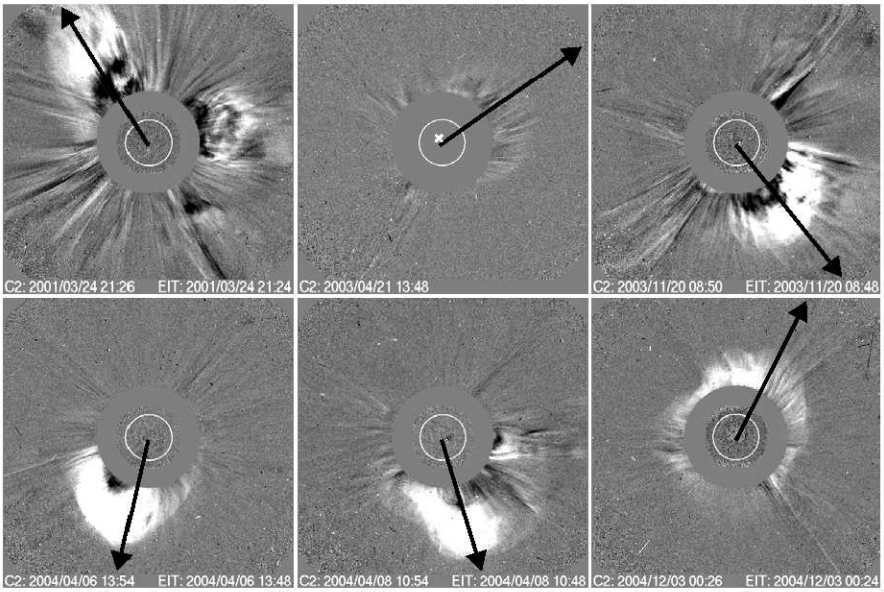

Figure 9. Snapshot images of the six CMEs associated with the driverless shocks (listed in Table 2). These are running difference images obtained by SOHO/LASCO using its inner coronagraph, C2. The white circle represents the optical Sun. Nearest EUV difference images (SOHO/EIT at 195 Å) are superposed, which show the solar sources of the CMEs. There was no EIT data for the 2003 April 21 CME, so the solar source is marked by 'x', which is the flare location obtained from the Solar Geophysical Data. The measurement position angle (MPA) is represented by the thick arrow. All though the CMEs appear as partial halos in these images, they eventually became full halos (asymmetric) in the LASCO C3 images, except for the 2003 April 21 CME. However, this CME is already faint, so it is difficult to say whether it is halo or not from C3 images. The CME on 2004 December 3 is already a halo in the C2 images.

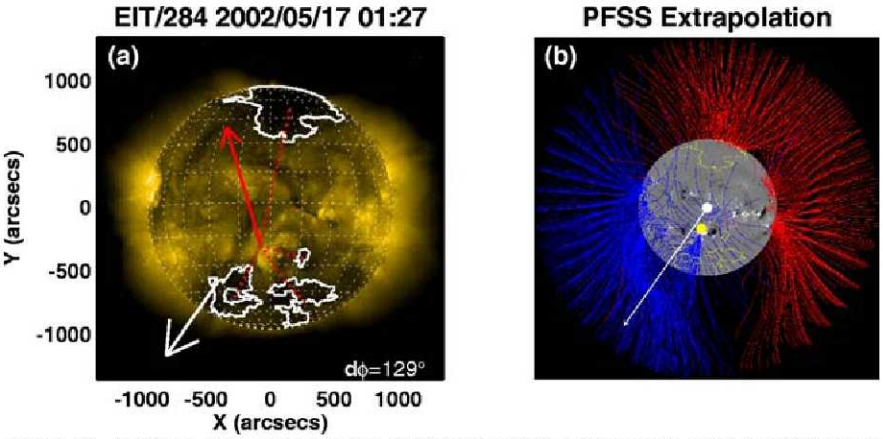

Figure 10. (left) The disk-center eruption of 2002 May 17 that did result in an IP shock followed by a driver on May 20 at 03:40 UT. The white arrow marks the MPA. The EIT 284 Å image shows two sets of coronal holes from near the north and south poles. The red arrow points from the solar source of the CME in the direction of the resultant influence

parameter (i.e., along the FPA). The dotted lines connect the eruption region to the centroids of the four coronal holes. (right) Potential field extrapolation of the photospheric field to the corona up to a heliocentric distance of 2.5 Rs. Red and blue lines denote field lines pointing towards and away from the Sun, respectively. Only open field lines are shown. The photospheric field shown is made from MDI synoptic maps updated every six hours. Note that the density of the field lines closer to the eruption region is high. The white arrow is along the MPA of the CME.

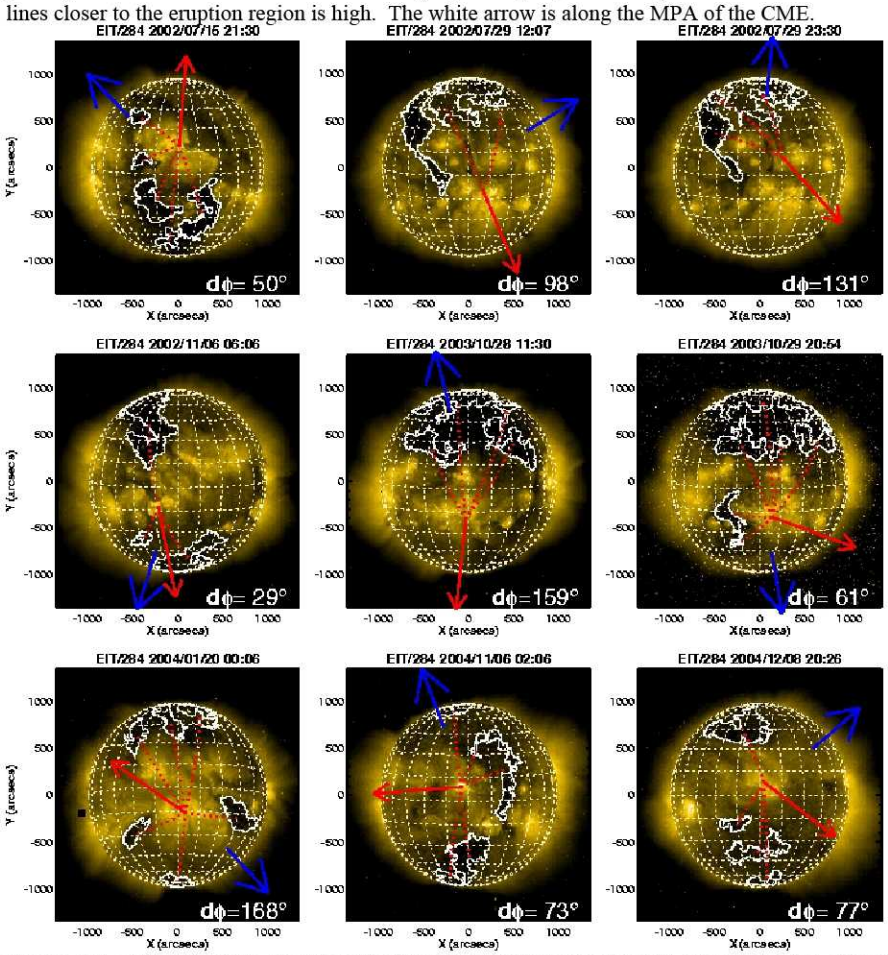

Figure 11a. First nine of the 18 disk-center CMEs resulting in shocks with drivers at 1 AU. The symbols are similar to the example shown in Fig.10. The difference (dφ) between MPA (blue arrow) and the FPA (red arrow) is shown for each case.

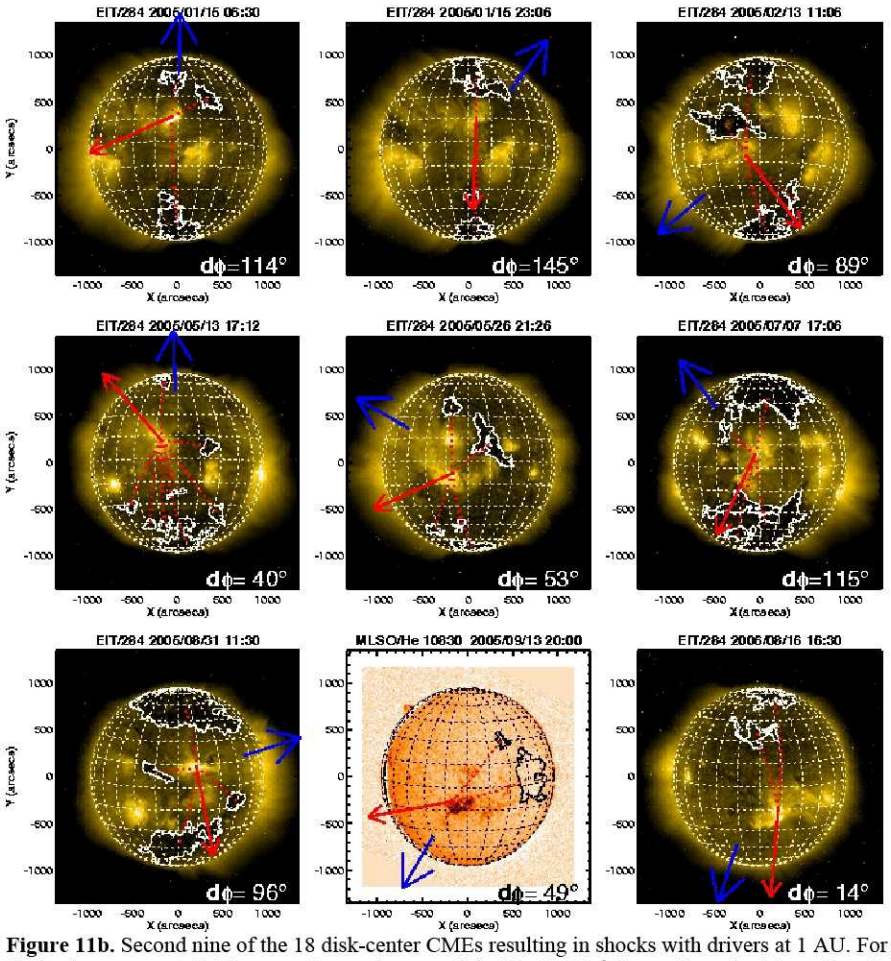

Figure 11b. Second nine of the 18 disk-center CMEs resulting in shocks with drivers at 1 AU. For the 2005 September 13 CME, there was an EIT data gap. So, we have used the He 10830 Å image from the Mauna Loa Solar Observatory. Coronal holes appear bright at this wavelength. The contour outlining the coronal hole encloses area in which the brightness exceeds the median brightness of the solar disk in the He 10830 Å image. As in other figures, the contour outlining coronal holes encloses regions in which the intensity is at or below the 50% of the median intensity of the solar disk in the EIT 284 Å images.

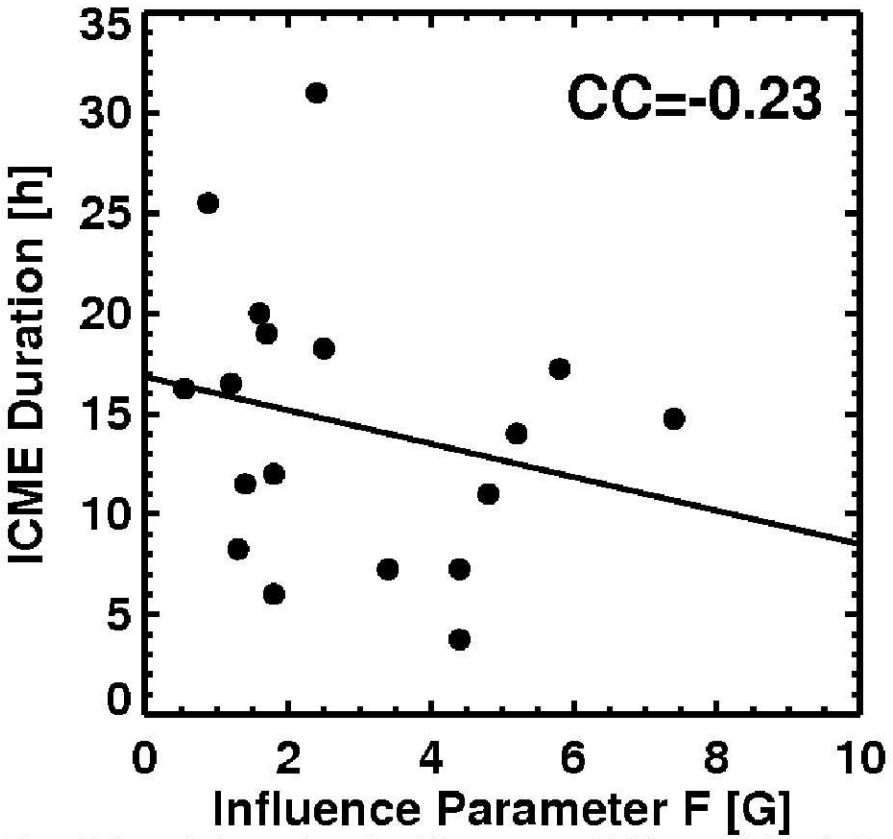

Figure 12. Scatter plot between the resultant influence parameter F of the coronal holes at the Sun and the duration of the ICMEs obtained from ACE data. The regression line and the correlation coefficient (CC = -0.23) are shown on the plot.